Granular Matter (2023) 25:77
https://doi.org/10.1007/s10035-023-01364-5

ORIGINAL REPORT

Investigating projectile penetration into immersed granular beds via CFD-DEM coupling

Jiayu Lin[1] · Tao Zhao[3] · Mingjing Jiang[1,2,4]

Received: 31 March 2023 / Accepted: 24 August 2023

Abstract
Projectile penetration into an immersed granular bed is a common phenomenon in both geophysics and engineering, encompassing various scenarios such as immersed crater formation and offshore soil-structure interaction. It involves the complex physical interaction between the fluid and granular materials. In this study, we investigate the dynamics of projectile penetration into a granular bed immersed in a fluid using a coupled computational fluid dynamics and discrete element method (CFD-DEM). The granular bed is composed of polydisperse particles, and the projectile is modeled as a rigid sphere. The morphology of crater formation, the dynamics of the projectile, and the drag force characteristics in immersed cases were studied in detail and compared to the dry scenario. The numerical results show that the final penetration depth of the projectile follows an empirical relation derived from experimental observations, where the falling height and the drag force during penetration obey a power-law function and a modified generalized Poncelet law, respectively. The interstitial fluid not only provides direct drag force, but also enhances the effective drag force of the granular bed by improving its generalized friction and effective viscosity in different configurations. Micro-analyses of the velocity evolution and contact force network in different stages of the fluid–solid interaction were performed to clarify the penetration dynamics. This research provides insights into the mechanisms of projectile penetration and the effects of interstitial fluid on granular media, which are crucial in engineering applications such as offshore anchoring, ball penetration tests in soft sediments, and soil-structure interactions.

Keywords CFD-DEM · Projectile penetration · Granular bed · Poncelet law · Drag force

1 Introduction

The dynamics of projectile penetration into granular beds have important implications across various fields of engineering, ranging from the formation of craters on planets to raindrops falling into granular media, and from rockfall impact to soil-structure interactions [1–5]. In the engineering geology discipline, this phenomenon has been extensively studied as it offers an ideal model to explore the rheology of grains under different flow and deformation regimes [6]. Related research includes the mechanism of rockfall impact against a granular soil buffering layer above a concrete/rock shed [7], the buffer capacity of granular matter to impact of the spherical projectile [8], and phenomenology identification of projectile penetration into soils [9]. In addition, this phenomenon is ubiquitous in geotechnics, such as cone penetration tests (CPT) [10], standard penetration test (SPT) [11], free fall penetrometers (FFP) [12], and the pile-soil interaction problem [13]. Recently, the behavior of robotic systems moving in soil has gained significant attention, as it is closely related to the interaction provided by ambient soil and employed on the moving intruder [14, 15]. The phenomenon is also observed widely in both geophysical and engineering situations for immersed scenarios, including the formation of underwater craters [16], the impact of asteroids in the ocean [17], and ocean engineering applications such as

✉ Tao Zhao
tao.zhao@brunel.ac.uk

✉ Mingjing Jiang
mingjing.jiang@mail.usts.edu.cn

1 School of Civil Engineering, Tianjin University, Tianjin 300072, China

2 School of Civil Engineering, Suzhou University of Science and Technology, Suzhou 215009, China

3 Department of Civil and Environmental Engineering, Brunel University London, London UB8 3PH, UK

4 College of Civil Engineering, Tongji University, Shanghai 200092, China

Published online: 22 September 2023

anchoring on sandy sea floors and ball penetration tests in soft sediment, where the dynamic of the intruder can be used to interpret the soil's properties [18]. Understanding the mechanisms underlying projectile penetration in immersed granular beds is crucial for a broad range of engineering applications, including the design of offshore structures, protective barriers, and soil characterization.

Albeit complex interaction and non-linear characteristics [19], numerous studies consisting of experiment, simulation, and theoretical analysis [20–23] have sought to understand the impact mechanism by identifying the projectile dynamic and observing how the medium responds to the impact load applied during the vertical impact, oblique impact [24, 25], and the dual impact [26, 27] duration, and the interaction mechanism is also explored. This includes craters formation [28], empirical scaling studies for dry grains [29, 30], and the experimental research on the projectile stopping time [1], illustrating the development of the network of force chains between solid grains during compression [31], and various other studies that apply macroscopic rheological models including jamming or shear thickening model to generalize the behavior of sand [32, 33]. Especially, in wet granular beds where the more complex interaction exists [34], the empirical scaling is also studied as a dry one while it observed that capillary forces between the grains modify the threshold level of fluidization and therefore impact dynamics [32, 35–37]. In addition, the unified power-law of the final penetration depth of a spherical intruder with low velocity penetrating dry and wet granular packings is introduced [38].

Up to now, the basic principle of a projectile impact with a granular medium immersed in liquid remains largely unexplored and the related fundamental research is still lacking. To study the impact of projectiles on submerged granular sediments, experimental studies have been conducted [39]. However, the intricate nature of interactions within the system has yet to be comprehensively understood, necessitating further investigations to establish connections between detailed micro-scale information and macro-scale phenomena, such as crater formation, velocity variations, and penetration depth laws. In addressing these distinctive granular characteristics, discrete element methods have emerged as a widely adopted approach. [38, 40, 41]. In particular, the coupled computational fluid dynamic-discrete element method (CFD-DEM) can be applied to study the complex solid–fluid interaction in immersed granular impact processes in geophysical and industrial settings. This approach offers superior computational convenience and accuracy in simulating fluid–solid interactions and has been used to simulate fluid-driven particle flow in various fields, including fluidization in chemistry [42], debris flow [43], sediment bed erosion [44] and submerged landslide [45]. The CFD-DEM modeling approach can also be extended to adapt to the polydispersity caused by the projectile and granular bed to simulate the impact of projectiles on submerged granular media.

In this study, the CFD-DEM modeling approach has been employed to investigate the projectile dynamics and drag force characteristics. This investigation encompasses an analysis of the constituents of the drag force as well as the internal synergistic mechanisms among the various components involved during the penetration process [41]. The paper is organized as follows: in the first section, the methodology of the extended CFD-DEM coupling approach has been discussed, with the focus on porosity calculation in a polydispersed granular system. Then, this approach has been adopted in performing simulations of the process of projectile impact on the immersed granular bed. Next, numerical results are analyzed in terms of the morphology of crater formation, projectile dynamics, drag force characteristics, and intrinsic mechanism. Discussions are carried out for the mechanism of the unique feature caused by the immersed condition, validation and comparison of the simulation results with classical theory, and new insight into the penetration dynamics. The conclusions are presented at the end of the article.

2 Methodology

2.1 The CFD-DEM coupling model

This study aimed to investigate the penetration of projectiles into an entirely immersed granular bed, specifically in a state referred to as the 'slurry state' [46]. In this state, the granular material is fully immersed and does not exhibit capillary action within the bulk [32]. Furthermore, the literature notes that capillary action is relevant only in the pendular state with saturations ranging from 0 to 30% [47]. For clarity and comparison, the published relevant research is summarized in Table 1. Previous experimental and simulated endeavors, as summarized below, encompass saturation levels spanning from 0 to 100% to scrutinize the impact response of wet/dry granular beds. In cases of partial saturation (< 100%), explicit consideration of capillary action is necessary. Conversely, in full saturation scenarios (100%), where capillary action is theoretically eliminated, instances like a sphere impacting a free surface-submerged granular bed (as compiled in Table 1) might lead to misleading outcomes due to capillary action linked to surface tension. This capillary action consistently emerges with the projectile and along the packing boundary, as underscored by the literature [36]. In addition, these aspects are often overlooked in the simulations [38], wherein the impact of interstitial water is typically addressed as a cohesive force due to the absence of an actual fluid. In the context of this work, the central focus lies on the scenario of complete immersion within a submarine

Table 1 A collection of published relevant research on granular impact

Study	Method	Case setup	Saturation	Free surface
Birch et al., [49]	Experiment	Wet	100%	Yes
Zhang et al., [34]	Experiment	Wet	8 ~ 80%	Yes
Marston et al., [32]	Experiment	Wet/dry	0 ~ 93.1%	Yes
Vo and Nguyen, [38]	Simulation	Wet/dry	-*	Yes
Brzinski et al., [36]	Experiment	Wet/dry	0 ~ 100%	Yes
Katsuragi and Durian, [1, 50]	Experiment	Dry	–	–
Tiwari et al., [41]	Simulation	Dry	–	–
Shen et al., [51]	Simulation	Dry	–	–
Grimaldi and Dressaire, [39]	Experiment	Submerged	100%	No
This study	Simulation	Submerged	100%	No

In the -*, the saturation is reflected by the cohesive stress in the range [0.0,351.94] Pa

environment, disregarding the influence of free surface tension [48].

For simulating the impact of projectiles on fully immersed granular media, the classical CFD-DEM model has been extended to be adaptive and accurately represent the behavior of non-spherical particles. The complete 3D contact model incorporating rolling/twisting resistances is applied in the DEM framework to capture the effects of particle angularity, assuming that two particles interact at a contact over a circular flat area. The shape parameter is used to account for the increase in the contact area and rolling resistance with higher angularity. More detailed information about the model can be found in the appendix.

The equations of motion for each particle in the system are derived from the second Newtonian law and are solved using the discrete element method. This approach allows the study of the complex solid–fluid interactions that occur during the impact of a projectile on a granular bed, including the formation of craters, velocity variation, and penetration depth law. By utilizing the CFD-DEM approach, the fluid–solid interaction and gain insights into the underlying physics of the impact process can be accurately simulated.

$$\begin{aligned} m_i \frac{\mathrm{d}\mathbf{U}_i^p}{\mathrm{d}t} &= \sum_{j=1}^{n_i^c} \mathbf{F}_{ij}^c + \mathbf{F}_i^f + \mathbf{F}_i^g \\ I_i \frac{\mathrm{d}\boldsymbol{\omega}_i}{\mathrm{d}t} &= \sum_{j=1}^{n_i^c} \mathbf{M}_{ij} \end{aligned} \tag{1}$$

where $\mathbf{U}_i^p$ denote the translational and $\boldsymbol{w}_i$ denote the angular velocity of particles i, respectively $\mathbf{F}_i^c$ and $\mathbf{M}_{ij}$ are the contact force and contact torque applied on the particle i by particle j or wall; n_i^c is the number of the contact associated with the particle. $\mathbf{F}_i^f$ is the particle–fluid interaction force acting on the particle i. $\mathbf{F}_i^g$ is the gravitational force of particles. m_i and I_i are the mass and moment of inertia of the particle i. In the CFD, the local-averaged Navier–Stokes equations are derived from well-known N-S equations by considering the existence of particles.

$$\begin{aligned} &\frac{\partial\left(\varepsilon\rho\mathbf{U}^f\right)}{\partial t} + \nabla\cdot\left(\varepsilon\rho\mathbf{U}^f\mathbf{U}^f\right) - \varepsilon\nabla\cdot\left(\mu_f\nabla\mathbf{U}^f\right) = -\nabla p - \mathbf{f}^p + \varepsilon\rho\mathbf{g} \\ &\frac{\partial(\varepsilon\rho)}{\partial t} + \nabla\cdot\left(\varepsilon\rho\mathbf{U}^f\right) = 0 \end{aligned} \tag{2}$$

where $\mathbf{U}^f$ is the average velocity of a fluid cell. p is the fluid pressure in the cell; μ_f is the viscosity of fluid; $\mathbf{f}^p$ is the interaction force owing to the particles in the cell on the fluid. $\mathbf{g}$ is the gravity vector. It is noted that the $\varepsilon = \mathrm{v}_{\mathrm{void}}/\mathrm{v}_{\mathrm{c}}$ denotes the porosity. The interaction force applied in this module includes two parts: the buoyancy force $\mathbf{F}^b$ and the drag force $\mathbf{F}.^d$ The drag force is calculated as the model proposed by Di Felice [14]

$$\begin{aligned} \mathbf{F}^d &= \frac{1}{8} C_d\,\rho\,\pi\,d_p^2\left(\mathbf{U}^f - \mathbf{U}^p\right)\left|\mathbf{U}^f - \mathbf{U}^p\right|\varepsilon^{-\chi} \\ C_d &= \left(0.63 + \frac{4.8}{\sqrt{\mathrm{Re}_p}}\right) \\ \mathrm{Re}_p &= \frac{\varepsilon\,\rho\,d_p\left|\mathbf{U}^f - \mathbf{U}^p\right|}{\mu_f} \\ \chi &= 3.7 - 0.65\exp\left[-\frac{(1.5 - \log_{10}\mathrm{Re}_p)^2}{2}\right] \end{aligned} \tag{3}$$

The buoyancy force is calculated as

$$\mathbf{F}^b = \frac{4}{3}\pi r^3\left(\nabla p - \rho_f\,\vec{\mathbf{g}}\right) \tag{4}$$

where d_p is the diameter of the considered particle. $\mathrm{C_d}$ is the drag coefficient, ρ_f is the fluid density, r is the particle radius, Re_p is the particle Reynolds number, and the χ is the empirical coefficient μ is the dynamic viscosity of the fluid.

The accuracy of fluid-particle interactions in local-averaged CFD-DEM simulations is heavily dependent on the

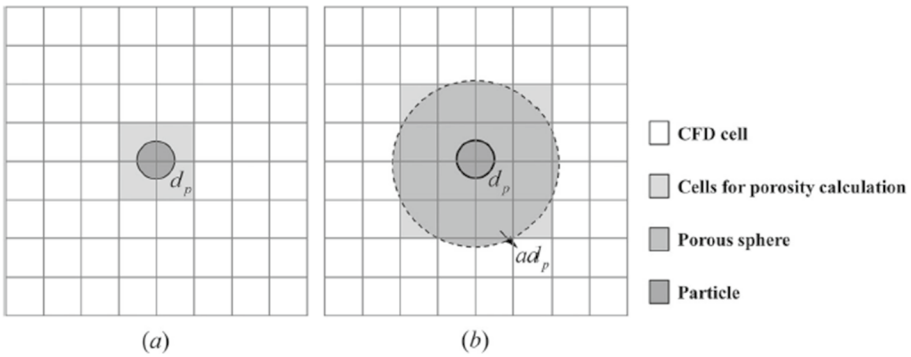

Fig. 1 Schematic of the porosity models. **a** Actual particle(divided model), **b** Porous sphere model (Cited and modified from Jing et al. [55])

Table 2 Fluid boundary conditions of the numerical simulations

Patch name	CFD boundary condition	DEM boundary condition
Bottom wall	U_f: 0	Fixed
	P: zero-gradient	
Top wall	U_f: zero-gradient	Fixed
	P: zero-gradient	
Fixed walls	U_f: 0	Fixed
	P: zero-gradient	

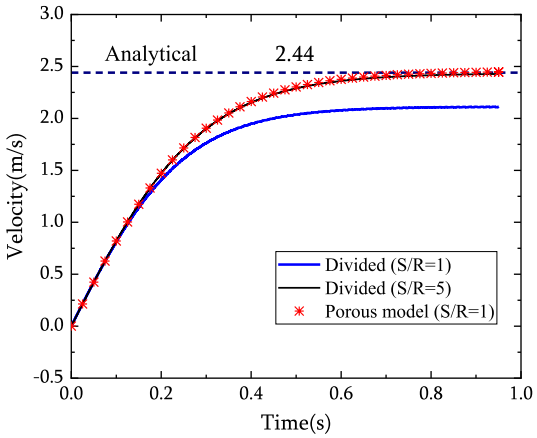

Fig. 2 Validation of 'projectile' correction

calculation of local porosity. Traditional porosity calculation methods, such as the centered model [52] and divided model [53], can lead to erroneous results when the maximum particle size is close to the fluid mesh size [54]. This is due to the discontinuities in the porosity field caused by the presence of large discrete particles. In this study, the accuracy and resolution of projectile dynamics are restricted by the size ratio of the projectile to mesh size. To overcome this limitation, an alternative method for calculating local porosities called the porous sphere model has been employed, which has been previously described in research [54, 55]. This method calculates the contribution of a particle to the local porosities not only in the cells where it is located but also in the cells that are centered within a larger region known as the porous area. For more details on the implementation of this method, please refer to the literature [54, 55]. A schematic diagram of the porous sphere model is shown in Fig. 1.

To validate the coupling model, a simulation of one particle sedimentation in water has been performed with the input parameters listed in Table 2 (in the next section on model configuration). Three simulations have been performed, with the varied ratio of the grid size to the particle size (S/R) and porosity calculation method, as presented in Fig. 2. The S/R = 1 cases are conducted respectively for the porous model and original divided calculation method where the volume of intersection of the cube representing the particle equally with the fluid element is calculated and adjusted to conserve the particle volume. The S/R = 5 case satisfies the basic assumption and corresponds to the ideal scenario. The results indicate that the porous model could produce quantitatively good results, agreeing well with the analytical result derived from the numerical solution of Stokes' law [56] and Divided (S/R = 5) results(as the ideal solution of mesh size ratio). On the contrary, the S/R = 1 case without the porous model correct would lead to a large discrepancy in final particle settling velocity. The numerical results could match well with observations in the literature [55].

2.2 Model configuration

The numerical model setup in this study incorporates insights from previous experiments and simulations [38, 41, 57] ensuring comprehensive consideration of boundary effects and size effects. The granular material employed in this study corresponds to the material used in previous work [58], which has undergone thorough calibration and extensive validation. The numerical model configuration of a projectile colliding onto a submerged granular bed is shown in Fig. 3a. The projectile is modeled as a rigid sphere of diameter (D) of 2.2 cm. The granular bed is

represented by an assembly of particles with GSD shown in Fig. 3b. The target granular bed composed of 120,000 particles is first prepared with UCM (under compaction multi-layer method) [59] to obtain the homogeneous initial state with a void ratio of 0.85. The container is composed of rigid walls with a length (L) equal to a width (W) of 22 cm and a height (H) of 15 cm. The non-dimensional parameters of W/D and L/D are 10.0, and H/D is 6.81, respectively, which are greater than 5.0 as suggested in the literature [57] for stable simulations. Therefore, the influence of model size on granular penetration can be neglected. After gravitational deposition, the densities of the granular bed ρ_g are 1453 kg/m^3 and 1895 kg/m^3, respectively for the dry and immersed wet conditions. The macroscopic granular friction angle is around 31° as calibrated in the former research [58]. In the context of immersed impact modeling, a projectile with a consistent prescribed velocity range (1 m/s to 6 m/s) is initially positioned beneath the water surface, closely adjacent to the surface of granular bed. In the current study, the granular bed is entirely immersed, resulting in the absence of any cohesive force and free surface tension [48]. It is noteworthy that the fluid domain is set up two times higher than the granular bed to create the immersed scenarios and avoid the size effect on the fluid domain [18]. Consequently, by setting the initial water height to a significantly large value, the simulated results remain unaffected by this parameter choice. The detailed boundary condition is set up as Table 2, which has been used and validated in the previous work [18]. The detailed input material parameters of the simulation are listed in Table 3.

Table 3 Parameters of the numerical simulations

	Parameter of model	Value
Bed particle	Effective modulus E_p/Pa	7e8
	Normal tangential stiffness ratio	5.0
	Anti-rotation coefficient	0.25
	Local crushing coefficient	0.5
	Friction coefficient	0.5
	Density ρ_g (kg/m^3)	2600
	Particle number	120,000
Projectile	Density ρ_p (kg/m^3)	7800
	Effective modulus E_p (Pa)	1e9
	Friction coefficient	0.5
	Normal tangential stiffness ratio	1.5
Fluid	Density, ρ_f(kg/m^3)	1000
	Kinetic viscosity, υ (m^2/s)	1.01e−6
	Mesh size (cm)	2.2×2.2×2.2

3 Results

3.1 Crater formation

Figure 4a1–a6 and b1–b6 illustrate the cratering process of projectile impact in the immersed and dry beds with the impact velocities ranging from 1 to 6 m/s, respectively. The plots show that the morphology of the submerged and dry craters caused by the projectile impact are both close to the conical while the dry one is with a larger opening. The affected area defined as the vertical displacement of particles exceeding the radius of the projectile is larger in the dry case, as illustrated in the top view. The ejection of particles in the immersed case is negligibly small, which is similar to

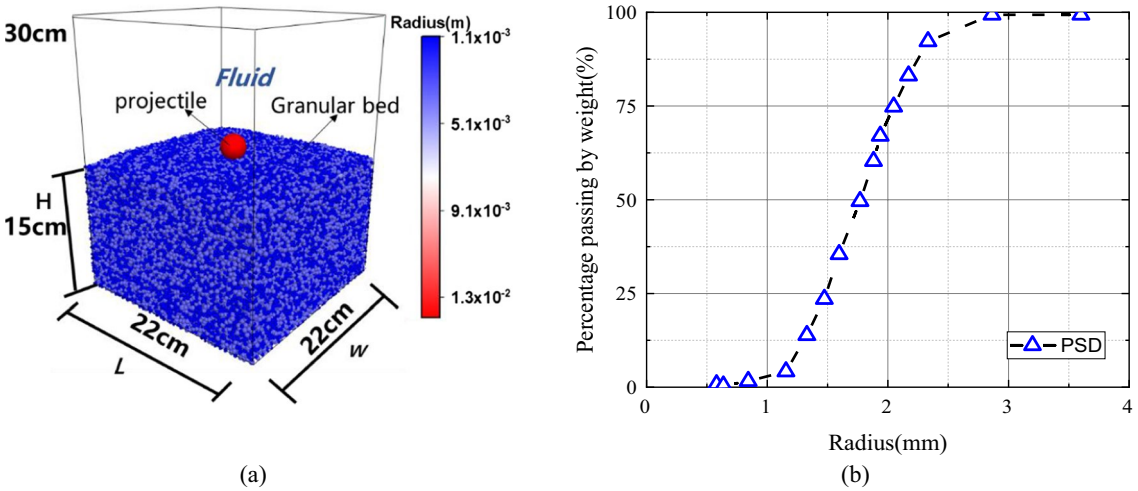

Fig. 3 **a** Numerical model configuration. Particles are colored according to the radius **b**-Grain size distribution (GSD) of granular bed

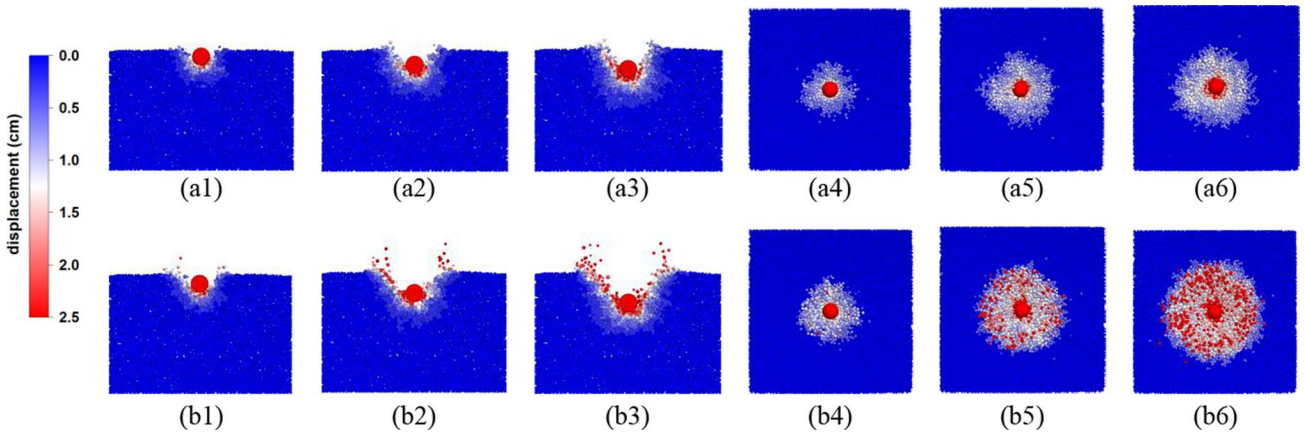

Fig. 4 The contour of the DEM model during the penetration process. The time interval between successive plots is 0.0035s, and the particles are colored according to the magnitude of the displacement. The series **a1**–**a3** are for the different initial velocities (2 m/s, 4 m/s, and 6 m/s) in immersed condition and the **b1–b3** are for the dry condition. **a1**–**a3** and **b1**–**b3** are the top-view snapshots of the granular bed corresponding to the vertical clip

the observations in the experimental test of the wet (saturated) granular bed [32] (seen in the inset plot of Fig. 5a). The distinct morphology in the experimental test is mainly induced by the cohesive force offered by the pore pressure while the phenomenon in this study can be potentially owing to the viscous effect from the interaction force offered by the water, which increases the resistance of particles motion. Figure 5a presents the evolution of the normalized depth ($[H] = h/D$) and diameter ($[D] = R/D$) of the crater, with the Froude number ($[V] = v_0/\sqrt{gD}$, g: the gravity acceleration). When the normalized impact velocity is less than 4.3, the evolution of $[H]$ is close in both two cases, during which the projectile exactly submerges into the granular bed totally and the opening forms initially. Whereas the results will diverge with increasing velocity, that $[H]$ in the dry case increases from 2.0 to 3.83, while in the immersed case, $[H]$ increased slower and is kept constant at about 2.5. Additionally, the distinct morphology of the craters could also be verified from the experimental results shown in the inset plot. For $[D]$, the same nonlinear relationship with the impact velocity is obtained, while for the immersed case, the increasing rate is smaller. The numerical results demonstrated a good agreement with well-documented experimental data for dry impact cases, as illustrated in Fig. 5b. From the viewpoint of energy, the geometry difference of the craters between the two cases implies different energy transition patterns. In the dry case, the mechanical energy of the projectile is mainly dissipated by the inter-friction between the particles in the granular bed [51] while in the immersed case, the fluid adds additional viscous energy consumption to both the projectile and granular bed. Thus, it is speculated that there is lower energy of the immersed system to create the crater. On the

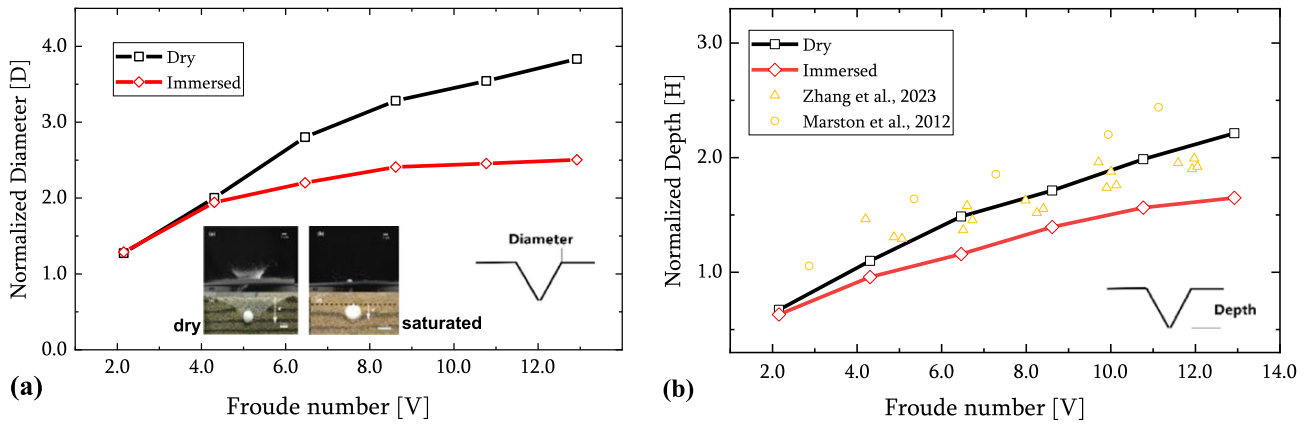

Fig. 5 The variation of normalized diameter (**a**) and normalized depth (**b**) of the crater for different initial velocities. The inset plot in (**a**) was adapted from [49] to reveal the different configurations (including particle ejection and morphology of the crater) between the dry and saturated case. The experimental data from the reference [32, 34] was included in (**b**) for comparison purposes

other hand, the special phenomenon inevitably depends on the granular dynamics, the momentum exchange, and the force transmission in the system consisting of the projectile, particles, and fluid, which will be discussed in the following sections.

3.2 Projectile dynamics

Figure 6a and b show respectively the time evolution of the normalized depth $[H](t)$ and the Froude number $[V](t)$ of the projectile. For the evolution of projectile penetration depth (Fig. 6a), both in the two cases it increases gradually to the final penetration depth, and the difference between the two cases is larger with the higher impact velocity (6m/s) but smaller with lower impact velocity (2m/s), which could also be observed from the crater analysis in Fig. 5b. As shown in Fig. 6b, at high impact speed, in both the immersed and dry cases, the penetration velocity decreases rapidly at the initial stage before the nearly t = 0.0025s, which is followed by a progressively decreasing period. At any specific time, the projectile motion in the immersed condition always has a lower velocity when compared with the dry cases. The curves of projectile velocity evolution in the two cases become close with decreasing initial impact velocity. It illustrates that the effect of interaction force provided by the fluid will be highlighted in the larger impact velocity condition, which is related to the positive correlation between the viscous force and velocity primarily reflected by Eq. (3). The relationship between the penetration depth and velocity is illustrated in Fig. 6c, and the classical function curve is plotted simultaneously for the two types of tests (dry, and immersed), which is also discovered in the experiment [50] and simulation [41]. All curves display the trend of a gradual transition from concave-down and concave-up shape. However, there is some divergence in progressive trend among the cases. Specifically, compared to the collected results the curve in immersed one decreases more rapidly during the whole process with a later turning point where the slope changes obviously, which is more distinct in the high impact velocity (6m/s). It could be found that this divergence gradually disappears with the decreasing impact velocity.

According to the literature [5], the final penetration depth of a projectile can be predicted by an empirical formula:

$$h = (0.14/\mu)(\rho_p/\rho_g)^{1/2} D^{2/3} H^{1/3} \tag{5}$$

where the μ is the macroscopic friction coefficient of particle assembly and H is the falling height calculated as $H = h + v_0^2/2g$. Figure 7a shows the scaling law between the final penetration depth and the total falling height. The solid curve and dash curve are the analytical results predicted by the empirical formula for the dry and immersed conditions, respectively. It is noted that in the immersed case, the density is considered as the saturation porous medium density as $\rho = \left(\rho_{solid} + \rho_{fluid} \times e\right)/(1+e)$, and the macroscopic friction coefficient of the granular bed particles is calculated as the tangent of the response angle (θ_r) mentioned above. As shown in Fig. 7a, for the dry case, the numerical results can match well with the empirical formula, demonstrating the accuracy of the empirical formula and the rationality of the numerical model. The immersed case can still match the empirical prediction, in which μ is determined through the fitting function as 0.71. The potential explanation for the origin of the increment in generalized 'friction' is that the fluid participation offers the external force resisting the particle motion and consequently produces more resistance to the projectile penetration. This seems to cause the increment of the shear resistance strength of the granular bed phenomenologically. Further discussion will be conducted in the drag force characteristics section.

Except for the empirical formula, the prevalent view that has emerged from the literature is that the projectile motion after impact can be assumed to follow the generalized Poncelet law [1, 60]:

$$m\ddot{h} = mg - F_n = mg - mv^2/l - kh \tag{6}$$

where h is the penetration depth of the projectile, m is the projectile mass; g is the gravity acceleration of value 9.8 m/

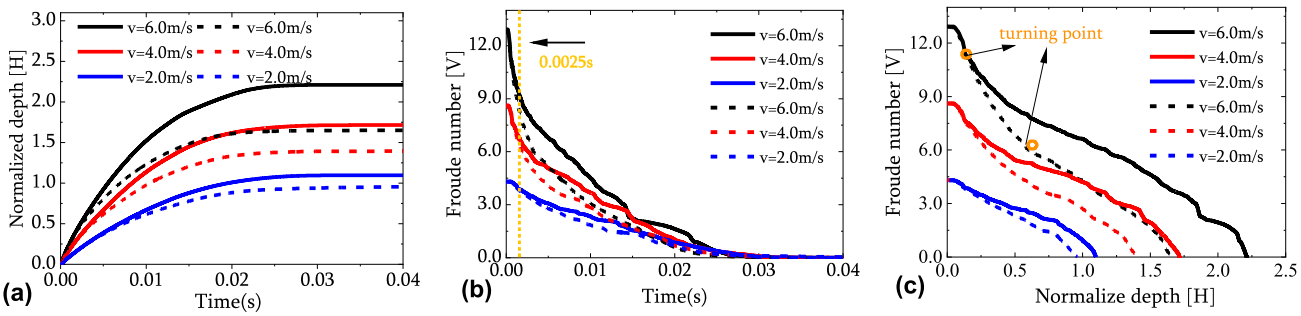

Fig. 6 Time evolution of the projectile **a** penetration depth and **b** velocity at different initial velocities for dry, immersed conditions. **c** The velocity of the projectile is a function of position. The dashed line stand for the immersed case while the solid line represents the dry case

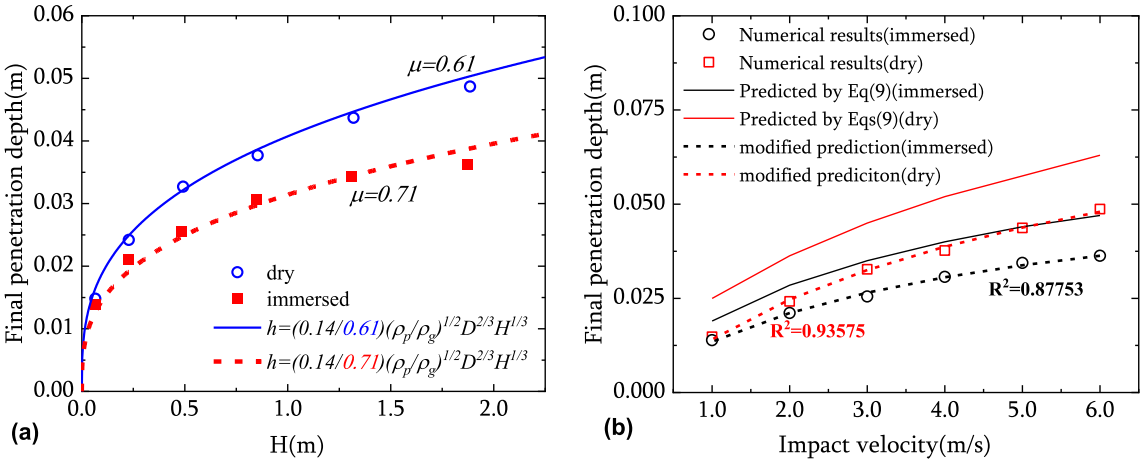

Fig. 7 **a** Relationship between the final penetration depth and the total falling height and the results predicted by the empirical formula. **b** Simulated results in both dry and immersed cases with the prediction and modified prediction from the general Poncelet law where the parameter is calibrated as Katsuragi and Durian [50]

s^2. According to Katsuragi and Durian [50], k (elastic constant of contact) and l (material parameter) can be approximately calculated respectively as:

$$k = 12mgD^{-1}\mu(\rho_g/\rho_p)^{1/2},\ l = D(0.25/\mu)\left(\rho_p/\rho_g\right) \tag{7}$$

The approach to determining μ and ρ is the same as used in Eq. (5) l and k are estimated as 0.0469 m and 62.18 N/m for the dry case and 0.0319 m and 81.35 N/m for the immersed condition. Equation (6) can be solved analytically as:

$$\frac{v^2}{v_0^2} = e^{-\frac{2h}{l}} - \frac{klh}{mv_0^2} + \left(\frac{gl}{v_0^2} + \frac{kl^2}{2mv_0^2}\right)\left(1 - e^{-\frac{2h}{l}}\right) \tag{8}$$

and the final penetration depth h is given when the limit of v approaches 0 [61], as:

$$h = \frac{l}{2} + \frac{mg}{k} + \frac{l}{2}W\left(\frac{2mv_0^2 - 2mgl - kl^2}{kl^2e^{1+2mg/kl}}\right) \tag{9}$$

where $W(x)$ is the Lambert W function as $W(x) = Xe^X$ and by substituting l, k, μ, and ρ, the final penetration depth of the projectile could be predicted and compared with the numerical results. The penetration depth predicted by the Poncelet law as Eq. (9) is shown in Fig. 7b. It can be seen that the results obtained are larger than the numerical results both in the dry and immersed conditions. This pattern is also observed in other simulations [51] and the reason is still unclear. The final fitting functions are $h^* = h - \left(0.00117v_0 + 0.0529\right)$ and $h^* = h - \left(0.000963v_0 + 0.00991\right)$ for the immersed and dry conditions, respectively. Hereafter, the increasing trend of variation derived from the numerical results is consistent with analytical results qualitatively and quantitatively indicating that the principle law of projectile motion in the immersed condition indeed resembles the dry one.

The stopping time is analyzed in Fig. 8. The threshold $v/v_0 = 0.005$ is proposed here and the inconsistency is eliminated [41]. As shown in Fig. 8, the stopping time undergoes a rapid decline when the impact velocity is low (v < 1.5m/s) and is gradually stabilized at 0.032 s. The process of change leads to no significant dependence between the stopping time and impact velocity at high impact velocity, which is also pointed out by other research [41]. It can be observed that the final stopping time is almost the same in both immersed and dry scenarios at a constant

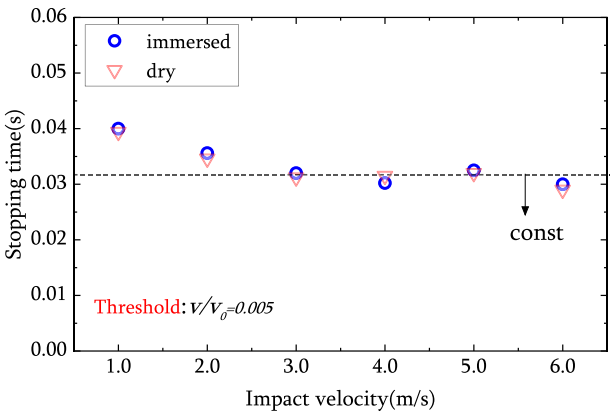

Fig. 8 The relationship between the stopping time and the initial velocity

value, which shows the independence of the modeling scenarios.

3.3 Drag-force characteristics

In an immersed granular bed, the drag force acting on the projectile is exerted by both the fluid and the assembly of granular particles. This phenomenon can be examined using the generalized form of Poncelet's law as:

$$m\ddot{h} = mg - F = mg - f(h) - C_d(h)\dot{h}^2 \tag{10}$$

The normal resistance force F is explicitly divided into the component related to the displacement $f(h) = kh$ and the component proportional to the velocity. The unbalanced force except for gravity in immersed impact is presented in Fig. 9a1–a3. It can be observed that the drag force provided by the fluid is fitted well by the proportionality constant C_d as 0.2, while the coefficient C_d of effective drag force offered by the contact with the granular bed is 3.5. Meanwhile, the major discrepancy emerges at low impact velocity on account of neglecting the $f(h) = kh$ with larger penetration depth. The C_d of the fluid is smaller than C_d of the granular as Fig. 9a1–a3 identified, which demonstrates the significant difference in rheology characteristics and shear resistance between the fluid and granular flow. The effective drag force directly provided by the inter-particle contact under dry and immersed conditions is compared in Fig. 9b1–b3, and it is seen that the drag force from the contact in the dry status is smaller than that in the immersed status as shown in this figure. Meanwhile, C_d declines from 3.5 to 2.1, meaning a decrease in

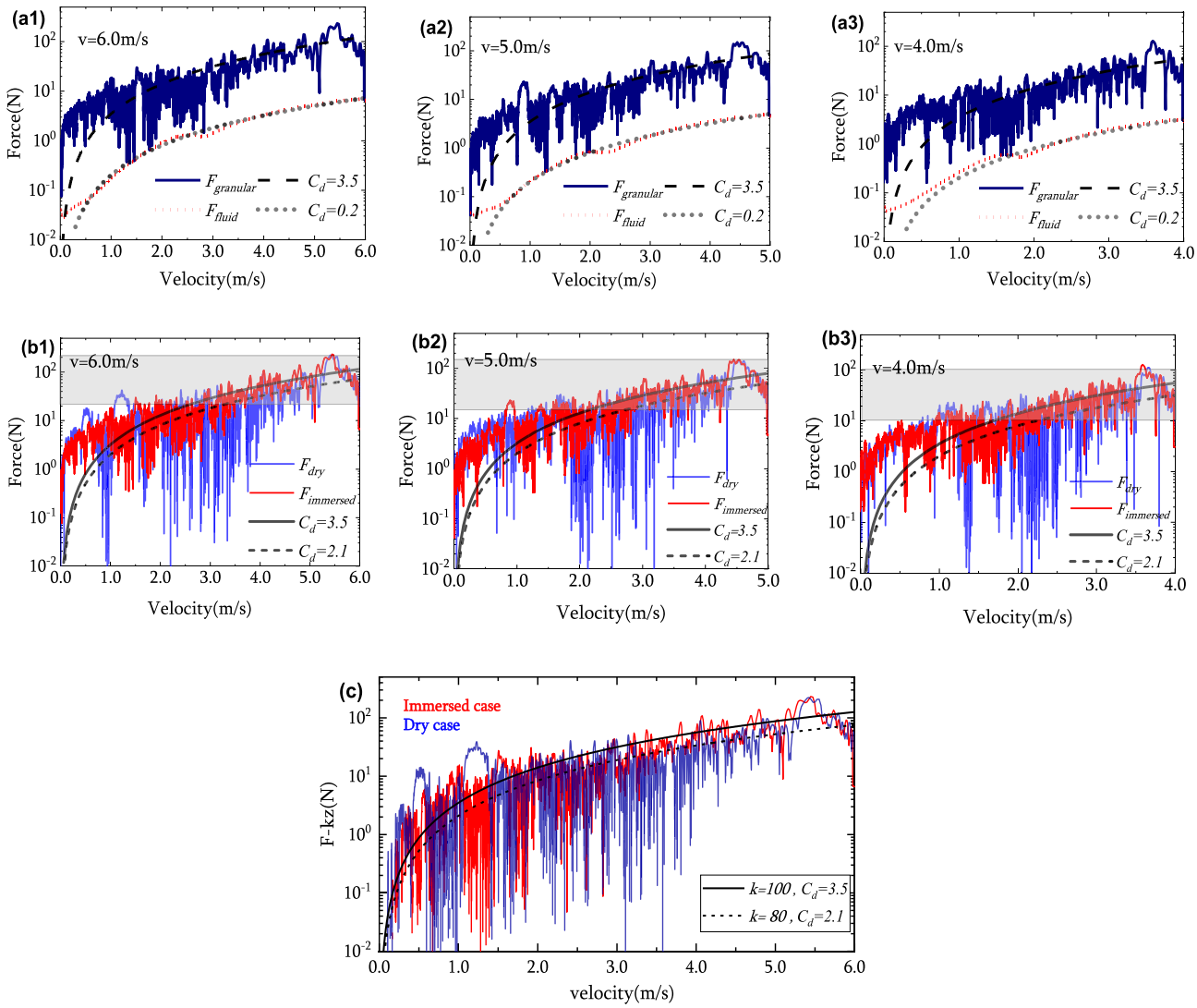

Fig. 9 **a1**–**a3** Drag force between the fluid and particle interaction in the immersed case. **b1**–**b3** Comparison of effective drag force between the two(immersed, dry) conditions. **c** The velocity-dependent part of the drag force, acting on the projectile, in two states respectively

apparent 'viscosity'. Figure 9c exhibits a notable fitting of the velocity-dependent drag force throughout the entire process, achieved by incorporating the depth-dependent fraction $f(h) = kh$ into the total drag force F. This fitting indicates that the depth-dependence fraction of the drag force plays a significant role in deeper positions, particularly when subjected to low velocities.

The following scaling law proposed by [50] could be used to check the fitting parameter.

$$k \sim \mu \left(\frac{\rho_g}{\rho_p}\right)^{1/2} \frac{mg}{D} \tag{11}$$

$$C_d(h) = C_d \sim \left(\frac{m\mu}{D}\right)\left(\frac{\rho_g}{\rho_p}\right) \tag{12}$$

The values of k and C_d are calibrated as 80 and 2.1, respectively in the dry condition, while they are 100 and 3.5 respectively in the immersed condition. It can be seen that the qualitative trend derived from Eqs. (11) and (12) agree well with the results achieved through the fitting curves. Specifically, the correlation among the k, C_d, and ρ_g, μ is consistent with the scaling law above. The k and C_d are positively correlated with the macroscopic friction coefficient μ and granular bed density ρ_g.

3.4 Mechanism analysis

The mechanism analysis of the projectile impact process in the immersed case includes the projectile dynamics in Fig. 10 and the multi-physical field evolution in Fig. 11. To investigate the detailed intruding process for cases with high initial impact velocity (5 m/s), the projectile impact has been divided into different stages, as illustrated in Fig. 10. During the initial contact stage (t < 0.001 s), the velocity rapidly decreases after impact, accompanied by a sharp increase in contact force, as shown in Fig. 10b. In this stage, the penetration depth is approximately 1/8 of the projectile diameter. Interestingly, Fig. 10a and b demonstrate that this process is independent of environmental conditions, as it is observed in both dry and immersed cases. For the physical field, during the initial contact stage, the excess pore pressure is negative in the hemisphere area close to the projectile, while the rest of the pore fluid field shows a positive excess pore pressure, as shown in the right of Fig. 11a. As the projectile moves

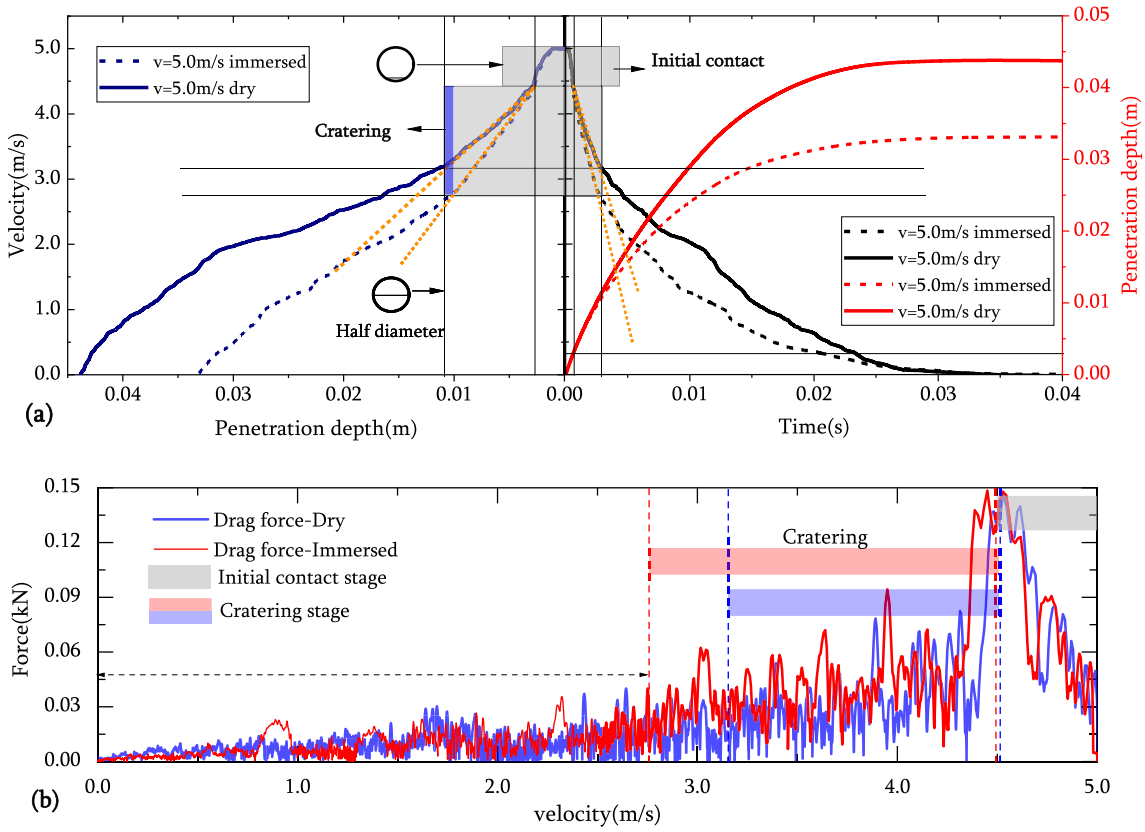

Fig. 10 **a** The different stages in the penetration duration with initial impact velocity (5m/s) where the common vertical axis is the transit velocity and **b** the stage identification in the Force versus velocity curve where the delimited line is marked as a vertical dashed line (blue denotes the dry case and red denotes the immersed case

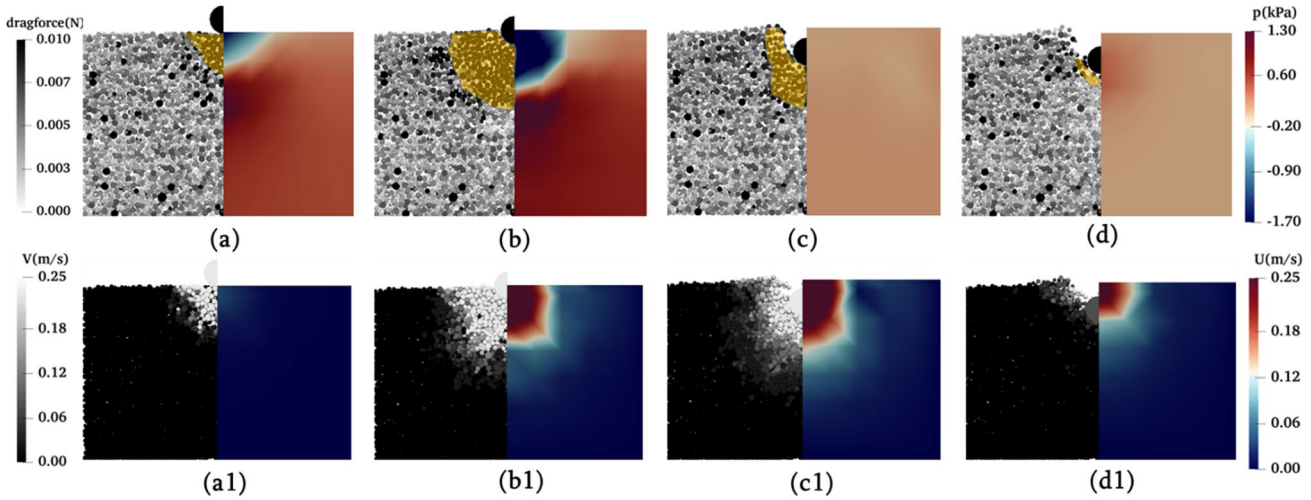

Fig. 11 The series are snapshots of the **a**–**d** vertical direction component of fluid-particle interaction force applied on the granular bed and excess of pressure in the fluid domain, **a1**–**d1** the velocity field including the particles and the fluid in the same range. **a**, **a1** t = 0.0005s **b**, **b1** t = 0.0025s **c**, **c1** t = 0.015s **d**, **d1** t = 0.02s

downward, the particles below experience a drag force from the surrounding fluid, which is most significant in the hemispherical region surrounding the contact points (highlighted as yellow in the left of Fig. 11a). This is also where a large velocity difference between the fluid and particles can be observed (as shown in Fig. 11a1). During the next stage marked in Fig. 10, which occurs from 0.001 to 0.003 s, the penetration depth reaches a value that is nearly equal to the radius of the projectile. This stage is known as the cratering process, which corresponds to the opening of the initial intact crater. Figure 10b shows that the drag force exhibits a positive correlation with velocity in both dry and immersed cases, which deviates from the initial contact stage. Furthermore, noticeable discrepancies arise between the drag forces observed in immersed and dry cases, suggesting the influence of external viscous effects from the fluid in this stage. This observation is supported by the analysis of the drag force composition in the preceding section. In this process, both in immersed and dry conditions, the curve slope of V(t) and Z(v) remained relatively stable, as indicated by the yellow dashed line in Fig. 10a. However, after the cratering stage, there was an intense change and transition into the next stage, which is consistent with previous simulations reported by Tiwari et al. [41]

For the physical field, during the cratering stage, High-pressure gradients of pore pressure emerge around the projectile, and the fluid flow is accelerated, as shown in Fig. 11b and b1, respectively. In addition, more particles beneath the projectile were accelerated to high velocity compared to the initial contact stage, indicating a larger affected area there. Correspondingly, in Fig. 11, the yellow region highlights an increase in the number of particles experiencing an upward drag force, indicative of significant viscous effects. Consequently, this greater resistance is observed in the immersed case compared to the dry case. In the third stage, the projectile consistently penetrated the granular bed in the already-opened crater. The velocity of the fluid increased and then decreased as excess pore pressure dissipated, as displayed in Fig. 11d and d1. The area of the hemispherical region that includes particles with high velocity decreased, and the magnitude of drag force in the granular bed dropped, leading to a stable state of the entire system. When $t > 0.035$ s, the projectile came to a stop, and the velocity of both fluid and granular bed particles decreased to zero, with the ejected bed particles resettling back into the bed.

Figure 12 provides further analysis of the penetrating process, specifically the force-chain variation with time, plotted in the range of 0.0–0.5 N. As shown in Fig. 12a, immediately after impact, the impact shock caused by the projectile develops in the region near the contacting point. During this stage, the projectile needs to overcome the initial stable force-chain network. In Fig. 12b, it is apparent that the force chain beneath the projectile is dispersed, indicating fluidization of the region [41]. However, the force chain is more complete in the immersed scenario shown in Fig. 12b1, illustrating that viscosity provided by the fluid weakens the fluidization phenomenon, especially underneath the projectile (as highlighted in the yellow region), resulting in more contact. Compared to the initial state, the projectile experiences a stronger velocity-dependent interaction during this stage. While the velocity-dependent drag force is still dominant, as indicated by the good fitting results in Fig. 9b2, it becomes weaker as the velocity decreases. After the cratering stage, the velocity of the granular bed declined with the decreasing projectile velocity, when the viscous

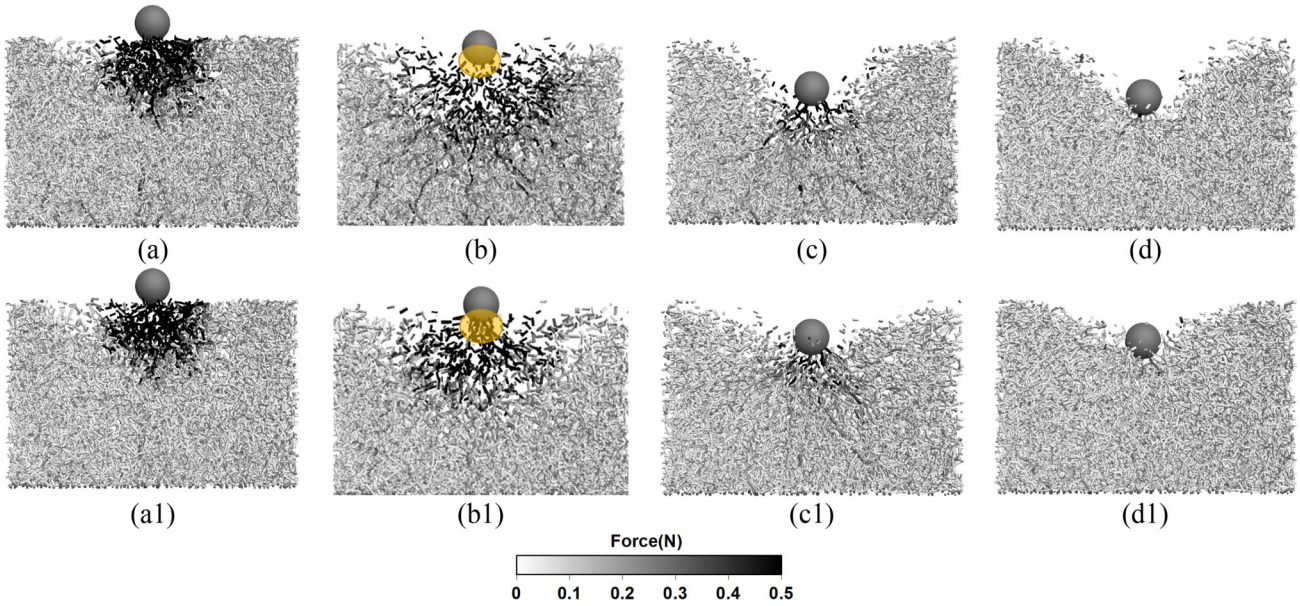

Fig. 12 The evaluations of force chains during the impact process (v = 5.0m/s). Note that the threshold is 0.5N. **a**, **a1** t = 0.0005s **b**, **b1** t = 0.0025s **c**, **c1** t = 0.015s **d**, **d1** t = 0.03s. **a**–**d** are in dry condition **a1**–**d1** are in immersed condition

effect provided by the fluid is nearly negligible, and the force network gradually recovers as plotted in Fig. 12c-d. During this stage, the depth-dependent drag force becomes more significant, as shown by the analysis in Fig. 9c.

4 Conclusions

In this paper, the CFD-DEM simulations have been used to investigate the impact of granular materials in immersed and corresponding dry environments. By analyzing the crater formation, projectile dynamics, drag force characteristics, and intrinsic mechanisms including multi-physical field evolution, a comprehensive understanding of the immersed granular impact process has been obtained. The macro-scale simulation results are in qualitative agreement with experimental observations. This research study yields the following key conclusions:

1) The morphology of the impact crater formed in the immersed scenario differs from the dry scenario, appearing conical with a smaller opening. The relationship between the shape parameter and impact velocity is nonlinear in both cases, but the D_N eventually rises to a stable value in the immersed case, with fewer particles ejected.
2) As the impact velocity increases, the final penetration depth in the immersed scenario is smaller than dry case, with the projectile velocity decreasing more rapidly. However, the stopped time shows no significant dependence on impact velocity. The modified Poncelet law, with the addition of a velocity dependence correction term, agrees well with the numerical results.
3) The immersed scenario exhibits a larger coefficient of the velocity-dependent and depth-dependent drag forces, due to the additional density and "viscosity" resulting from the interaction between the fluid and particles.
4) The intrinsic mechanism of the immersed impact condition has been investigated by dividing the process into three stages based on the dynamic behavior characteristics. In each stage, the evolution of the fluid field, bed granular motion, and force chain have been identified. The analysis demonstrates the fluid's viscous effect at different scales.

Overall, the research provides valuable insights into the complex dynamics of immersed granular impacts, which have implications for a range of practical applications in fields such as geology, civil engineering, and material science.

Appendix: The complete 3D contact model incorporating rolling/twisting resistances

In this Appendix, the mechanism of the complete three-dimensional (3D) contact model incorporating rolling/twisting resistances is shown below. The main features of the model are that (1) the contact behavior was physically

derived and (2) only two additional parameters, shape parameter β (linking the contact area radius and particle size) and local crushing parameter ζc (describing local contact crushing resistance) were introduced when compared with the standard 3D DEM. The schematic of the local Cartesian coordinate system and the relative velocities and rotation rates at a contact area are shown in Fig. 13a. Figure 13b presents the vectors used in the model implementation **n** as the unit vector in the contact normal direction, and $\dot{\mathbf{U}}_\mathbf{n}$, $\dot{\mathbf{U}}_\mathbf{s}$, $\dot{\boldsymbol{\omega}}_\mathbf{r}$, and $\dot{\omega}_t$ are the relative normal velocity, tangential velocity, rolling rate, and twisting rate respectively. Further detailed information and validation of the complete model could be found in the literature[62]

The mechanical responses will be obtained from the analysis of the process where the contact component is loaded undergoing the different generalized displacements and the mechanical responses of the contact model are plotted in Fig. 14

As Fig. 14 shows, the peak resistance in the shear, rolling, and twisting directions are controlled by the normal force multiplied by the $\zeta_c\overline{R}/4$ and $0.65\mu\overline{R}$ respectively. The derived formulations for the contact behavior are demonstrated in Table 4, which are implemented to control the force–displacement law in the DEM model.

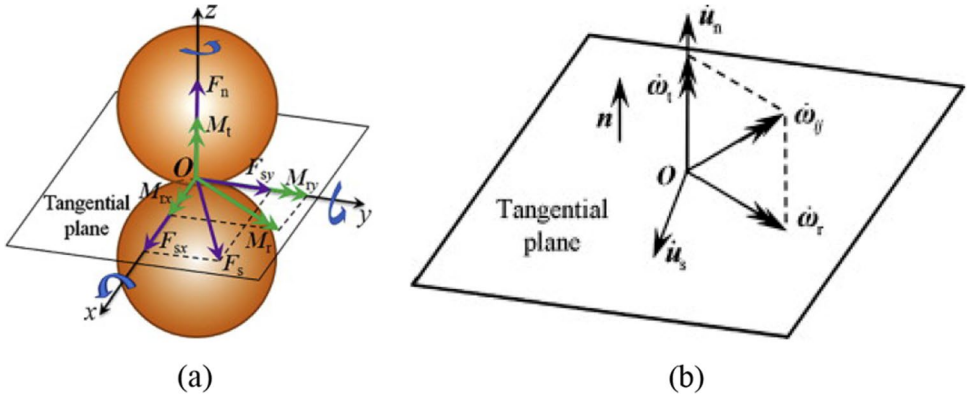

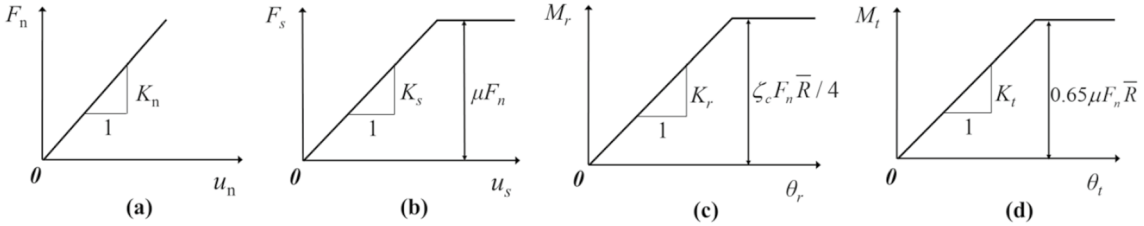

Fig. 13 **a** The local Cartesian coordinate system **b** The relative velocities and rotation rates

Fig. 14 Mechanical responses of the 3D complete contact model: **a** normal direction, **b** tangential direction, **c** rolling direction, and **d** twisting direction

Table 4 Force–displacement law in the complete 3D contact model

	Contact response	stiffness	Peak resistance	Damping response	Damping coefficient
Normal	$\boldsymbol{F}_n = K_n u_n \boldsymbol{n}$	K_n	–	$\boldsymbol{F}_n^v = -c_n 2\dot{\boldsymbol{u}}_n$	c_n
Tangential	$\boldsymbol{F}_s \leftarrow \boldsymbol{F}_s + K_s 2\dot{\boldsymbol{u}}_s \Delta t$	K_s	uF_n	$\boldsymbol{F}_s^v = -c_n 2\dot{\boldsymbol{u}}_s$	c_s
Rolling	$\boldsymbol{M}_r \leftarrow \boldsymbol{M}_r + K_r 2\dot{\boldsymbol{\omega}}_r \Delta t$	$K_r = 0.25 K_n \overline{R}^2$	$\zeta_c F_n \overline{R}/4$	$\boldsymbol{M}_r^v = -c_r 2\dot{\boldsymbol{\omega}}_r$	$c_r = 0.25\overline{R}^2 c_n$
Twisting	$\boldsymbol{M}_t \leftarrow \boldsymbol{M}_t + K_t 2\dot{\boldsymbol{\omega}}_t \Delta t$	$K_t = 0.25 K_s \overline{R}^2$	$0.65\mu F_n \overline{R}$	$\boldsymbol{M}_t^v = -c_t 2\dot{\boldsymbol{\omega}}_t$	$c_t = 0.5\overline{R}^2 c_s$

Acknowledgements This research was supported, in whole or in part, by the Major Program of National Natural Science Foundation of China (Grant No. 51890911), the UK Engineering and Physical Sciences Research Council (EPSRC) New Investigator Award (Grant No. EP/V028723/1), Hainan Province Science and Technology Special Fund (Grant No. ZDYF2021SHFZ264), and the State Key Laboratory of Disaster Reduction in Civil Engineering (Grant No. SLDRCE19-A-06). The datasets generated during and/or analysed during the current study are available from the corresponding author on reasonable request

Declarations

Conflict of interest The authors declare that they have no conflict of interest.

References

1. Katsuragi, H., Durian, D.J.: Unified force law for granular impact cratering. Nat. Phys. **3**, 420–423 (2007). https://doi.org/10.1038/nphys583
2. Deboeuf, S., Gondret, P., Rabaud, M.: Dynamics of grain ejection by sphere impact on a granular bed. Phys. Rev. E **79**, 041306 (2009). https://doi.org/10.1103/PhysRevE.79.041306
3. Brzinski, T.A., Mayor, P., Durian, D.J.: Depth-dependent resistance of granular media to vertical penetration. Phys. Rev. Lett. **111**, 168002 (2013). https://doi.org/10.1103/PhysRevLett.111.168002
4. Marston, J.O., Thoroddsen, S.T., Ng, W.K., Tan, R.B.H.: Experimental study of liquid drop impact onto a powder surface. Powder Technol. **203**, 223–236 (2010). https://doi.org/10.1016/j.powtec.2010.05.012
5. Uehara, J.S., Ambroso, M.A., Ojha, R.P., Durian, D.J.: Low-speed impact craters in loose granular media. Phys. Rev. Lett. **91**, 194301 (2003). https://doi.org/10.1103/PhysRevLett.91.149902
6. van der Meer, D.: Impact on granular beds. Annu. Rev. Fluid Mech. **49**(49), 463–484 (2017). https://doi.org/10.1146/annurev-fluid-010816-060213
7. Shen, W.G., Zhao, T., Dai, F., Jiang, M.J., Zhou, G.G.D.: DEM analyses of rock block shape effect on the response of rockfall impact against a soil buffering layer. Eng. Geol. **249**, 60–70 (2019). https://doi.org/10.1016/j.enggeo.2018.12.011
8. Yan, Y., Li, P., Ji, S.: Buffer capacity of granular matter to impact of spherical projectile based on discrete element method. Front. Struct. Civ. Eng. **7**, 50–54 (2013). https://doi.org/10.1007/s11709-013-0186-x
9. Omidvar, M., Malioche, J.D., Bless, S., Iskander, M.: Phenomenology of rapid projectile penetration into granular soils. Int. J. Impact Eng. **85**, 146–160 (2015). https://doi.org/10.1016/j.ijimpeng.2015.06.002
10. Lim, Y.X., Tan, S.A., Phoon, K.-K.: Friction angle and overconsolidation ratio of soft clays from cone penetration test. Eng. Geol. **274**, 105730 (2020). https://doi.org/10.1016/j.enggeo.2020.105730
11. Kuo, Y.-S., Chong, K.-J., Tseng, Y.-H., Hsu, C.-W., Lin, C.-S.: Assessment on liquefaction potential of seabed soil in Chang-Bin Offshore wind farm considering parametric uncertainty of standard penetration tests. Eng. Geol. **267**, 105497 (2020). https://doi.org/10.1016/j.enggeo.2020.105497
12. Jaber, R., Stark, N., Jafari, N., Ravichandran, N.: Combined portable free fall penetrometer and chirp sonar measurements of three texas river sections post hurricane harvey. Eng. Geol. **294**, 106324 (2021). https://doi.org/10.1016/j.enggeo.2021.106324
13. Hu, X., Liu, D., Niu, L., Liu, C., Wang, X., Fu, R.: Development of soil–pile interactions and failure mechanisms in a pile-reinforced landslide. Eng. Geol. **294**, 106389 (2021). https://doi.org/10.1016/j.enggeo.2021.106389
14. Zhang, N., Fuentes, R.: Horizontal penetration of a finite-length intruder in granular materials. Granul. Matter. **24**, 122 (2022). https://doi.org/10.1007/s10035-022-01281-z
15. Martinez, A., Dejong, J., Akin, I., Aleali, A., Arson, C., Atkinson, J., Bandini, P., Baser, T., Borela, R., Boulanger, R., Burrall, M., Chen, Y., Collins, C., Cortes, D., Dai, S., DeJong, T., Dottore, E.D., Dorgan, K., Fragaszy, R., Frost, J.D., Full, R., Ghayoomi, M., Goldman, D.I., Gravish, N., Guzman, I.L., Hambleton, J., Hawkes, E., Helms, M., Hu, D., Huang, L., Huang, S., Hunt, C., Irschick, D., Lin, H.T., Lingwall, B., Marr, A., Mazzolai, B., McInroe, B., Murthy, T., O'Hara, K., Porter, M., Sadek, S., Sanchez, M., Santamarina, C., Shao, L., Sharp, J., Stuart, H., Stutz, H.H., Summers, A., Tao, J., Tolley, M., Treers, L., Turnbull, K., Valdes, R., Paassen, Lv., Viggiani, G., Wilson, D., Wu, W., Yu, X., Zheng, J.: Bio-inspired geotechnical engineering: principles, current work, opportunities and challenges. Geotechnique **72**, 687–705 (2022). https://doi.org/10.1680/jgeot.20.P.170
16. Jansa, L.F., Pe-Piper, G.: Identification of an underwater extraterrestrial impact crater. Nature **327**, 612–614 (1987). https://doi.org/10.1038/327612a0
17. Patchett, J.M., Samsel, F., Tsai, K., Gisler, G.R., Rogers, D.H., Abram, G., Turton, T.L., Alamos, L.: Visualization and analysis of threats from asteroid ocean impacts (2016)
18. Guo, X.S., Nian, T.K., Wang, D., Gu, Z.D.: Evaluation of undrained shear strength of surficial marine clays using ball penetration-based CFD modelling. Acta Geotech. **17**, 1627–1643 (2022). https://doi.org/10.1007/s11440-021-01347-x
19. Wada, K., Senshu, H., Matsui, T.: Numerical simulation of impact cratering on granular material. Icarus **180**, 528–545 (2006). https://doi.org/10.1016/j.icarus.2005.10.002
20. Newhall, K.A., Durian, D.J.: Projectile-shape dependence of impact craters in loose granular media. Phys. Rev. E Stat. Nonlin. Soft. Matter. Phys. **68**, 060301 (2003). https://doi.org/10.1103/PhysRevE.68.060301
21. Crassous, J., Beladjine, D., Valance, A.: Impact of a projectile on a granular medium described by a collision model. Phys. Rev. Lett. **99**, 248001 (2007). https://doi.org/10.1103/PhysRevLett.99.248001
22. Horabik, J., Sochan, A., Beczek, M., Mazur, R., Ryzak, M., Parafiniuk, P., Kobylka, R., Bieganowski, A.: Discrete element method simulations and experimental study of interactions in 3D granular bedding during low-velocity impact. Powder Technol. **340**, 52–67 (2018). https://doi.org/10.1016/j.powtec.2018.09.004
23. Nishida, M., Tanaka, Y.: DEM simulations and experiments for projectile impacting two-dimensional particle packings including dissimilar material layers. Granul. Matter **12**, 357–368 (2010). https://doi.org/10.1007/s10035-010-0173-z
24. Ye, X., Wang, D., Zhang, X., Zhang, C., Du, W., Su, X., Li, G.: Projectile oblique impact on granular media: penetration depth and dynamic process. Granul. Matter **23**, 48 (2021). https://doi.org/10.1007/s10035-021-01108-3

25. Wang, D., Zheng, X.: Experimental study of morphology scaling of a projectile obliquely impacting into loose granular media. Granul. Matter **15**, 725–734 (2013). https://doi.org/10.1007/s10035-013-0446-4
26. Jiménez-Valdez, M., Tomay, E., Marston, J.O., Pacheco-Vázquez, F.: Doublet craters originated by low speed impact experiments in granular matter. Granul. Matter **24**, 116 (2022). https://doi.org/10.1007/s10035-022-01279-7
27. Espinosa, M., Díaz-Melián, V., Serrano-Muñoz, A., Altshuler, E.: Intruders cooperatively interact with a wall into granular matter. Granul. Matter **24**, 39 (2022). https://doi.org/10.1007/s10035-021-01200-8
28. Guzman, I.L., Iskander, M., Bless, S.: Visualization of impact cratering in granular media using quarter space penetration tests. Granul. Matter **23**, 63 (2021). https://doi.org/10.1007/s10035-021-01131-4
29. Goldman, D.I., Umbanhowar, P.: Scaling and dynamics of sphere and disk impact into granular media. Phys. Rev. E **77**, 021308 (2008). https://doi.org/10.1103/PhysRevE.77.021308
30. Guzman, I.L., Iskander, M., Bless, S., Qi, C.: Terminal depth of penetration of spherical projectiles in transparent granular media. Granul. Matter **16**, 829–842 (2014). https://doi.org/10.1007/s10035-014-0528-y
31. Clark, A.H., Petersen, A.J., Behringer, R.P.: Collisional model for granular impact dynamics. Phys. Rev. E **89**, 012201 (2014). https://doi.org/10.1103/PhysRevE.89.012201
32. Marston, J.O., Vakarelski, I.U., Thoroddsen, S.T.: Sphere impact and penetration into wet sand. Phys. Rev. E **86**, 020301 (2012). https://doi.org/10.1103/PhysRevE.86.020301
33. Waitukaitis, S.R., Roth, L.K., Vitelli, V., Jaeger, H.M.: Dynamic jamming fronts. EPL **102**, 44001 (2013). https://doi.org/10.1209/0295-5075/102/44001
34. Zhang, X., Zhang, D., Wang, Y., Ji, S., Zhao, H.: Dynamic characteristics of sphere impact into wet granular materials considering suction. Granul. Matter **25**, 18 (2023). https://doi.org/10.1007/s10035-022-01304-9
35. Strauch, S., Herminghaus, S.: Wet granular matter: a truly complex fluid. Soft Matter **8**, 8271–8280 (2012). https://doi.org/10.1039/c2sm25883h
36. Brzinski, T.A., Schug, J., Mao, K., Durian, D.J.: Penetration depth scaling for impact into wet granular packings. Phys. Rev. E **91**, 022202 (2015). https://doi.org/10.1103/PhysRevE.91.022202
37. Waitukaitis, S.R., Jaeger, H.M.: Impact-activated solidification of dense suspensions via dynamic jamming fronts. Nature **487**, 205–209 (2012). https://doi.org/10.1038/nature11187
38. Vo, T.T., Nguyen, T.K.: Unified penetration depth of low-velocity intruders into granular packings. Phys. Rev. E **106**, 014902 (2022). https://doi.org/10.1103/PhysRevE.106.014902
39. Grimaldi, E., Dressaire, E.: Crater formation by sphere impact on a submerged granular bed. J. Vis. **19**, 577–579 (2016). https://doi.org/10.1007/s12650-016-0353-y
40. Carvalho, D.D., Lima, N.C., Franklin, E.M.: Roles of packing fraction, microscopic friction, and projectile spin in cratering by impact. Phys. Rev. E **107**, 044901 (2023)
41. Tiwari, M., Mohan, T.R.K., Sen, S.: Drag-force regimes in granular impact. Phys. Rev. E **90**, 062202 (2014). https://doi.org/10.1103/PhysRevE.90.062202
42. Jajcevic, D., Siegmann, E., Radeke, C., Khinast, J.G.: Large-scale CFD-DEM simulations of fluidized granular systems. Chem. Eng. Sci. **98**, 298–310 (2013). https://doi.org/10.1016/j.ces.2013.05.014
43. Kong, Y., Li, X.Y., Zhao, J.D., Guan, M.F.: Load-deflection of flexible ring-net barrier in resisting debris flows. Geotechnique (2023). https://doi.org/10.1680/jgeot.22.00135
44. Zheng, H.C., Shi, Z.M., Peng, M., Yu, S.B.: Coupled CFD-DEM model for the direct numerical simulation of sediment bed erosion by viscous shear flow. Eng. Geol. **245**, 309–321 (2018). https://doi.org/10.1016/j.enggeo.2018.09.003
45. Jiang, M.J., Sun, C., Crosta, G.B., Zhang, W.C.: A study of submarine steep slope failures triggered by thermal dissociation of methane hydrates using a coupled CFD-DEM approach. Eng. Geol. **190**, 1–16 (2015). https://doi.org/10.1016/j.enggeo.2015.02.007
46. Mitarai, N., Nori, F.: Wet granular materials. Adv. Phys. **55**, 1–45 (2006)
47. Chu, X., Zhu, Z., Wang, L.: Numerical investigation on the influence of water content on collapse of granular columns. Granul. Matter **25**, 37 (2023)
48. Jewel, R., Panaitescu, A., Kudrolli, A.: Micromechanics of intruder motion in wet granular medium. Phys. Rev. Fluids **3**, 084303 (2018)
49. Birch, S., Manga, M., Delbridge, B., Chamberlain, M.: Penetration of spherical projectiles into wet granular media. Phys. Rev. E **90**, 032208 (2014)
50. Katsuragi, H., Durian, D.J.: Drag force scaling for penetration into granular media. Phys. Rev. E **87**, 052208 (2013). https://doi.org/10.1103/PhysRevE.87.052208
51. Shen, W.G., Zhao, T., Crosta, G.B., Dai, F., Dattola, G.: Influence of inter-particle friction and damping on the dynamics of spherical projectile impacting onto a soil bed. Front. Earth Sci. **10**, 835271 (2022). https://doi.org/10.3389/feart.2022.835271
52. Zhao, J.D., Shan, T.: Coupled CFD-DEM simulation of fluid-particle interaction in geomechanics. Powder Technol. **239**, 248–258 (2013). https://doi.org/10.1016/j.powtec.2013.02.003
53. Kloss, C., Goniva, C., Hager, A., Amberger, S., Pirker, S.: Models, algorithms and validation for opensource DEM and CFD-DEM. Prog. Comput. Fluid Dyn. **12**, 140–152 (2012). https://doi.org/10.1504/Pcfd.2012.047457
54. Link, J.M., Cuypers, L.A., Deen, N.G., Kuipers, J.A.M.: Flow regimes in a spout-fluid bed: a combined experimental and simulation study. Chem. Eng. Sci. **60**, 3425–3442 (2005). https://doi.org/10.1016/j.ces.2005.01.027
55. Jing, L., Kwok, C.Y., Leung, Y.F., Sobral, Y.D.: Extended CFD-DEM for free-surface flow with multi-size granules. Int. J. Numer. Anal. Meth. Geomech. **40**, 62–79 (2016). https://doi.org/10.1002/nag.2387
56. Batchelor, G.K.: An introduction to fluid dynamics. Cambridge University Press, Cambridge (1967)
57. Seguin, A., Bertho, Y., Gondret, P.: Influence of confinement on granular penetration by impact. Phys. Rev. E **78**, 010301 (2008). https://doi.org/10.1103/PhysRevE.78.010301
58. Jiang, M.J., Sun, R.H., Arroyo, M., Du, W.H.: Salinity effects on the mechanical behaviour of methane hydrate bearing sediments: a DEM investigation. Comput. Geotech. **133**, 104067 (2021). https://doi.org/10.1016/j.compgeo.2021.104067
59. Jiang, M.J., Konrad, J.M., Leroueil, S.: An efficient technique for generating homogeneous specimens for DEM studies. Comput. Geotech. **30**, 579–597 (2003). https://doi.org/10.1016/S0266-352x(03)00064-8
60. Seguin, A., Bertho, Y., Gondret, P., Crassous, J.: Sphere penetration by impact in a granular medium: a collisional process. EPL **88**, 44002 (2009). https://doi.org/10.1209/0295-5075/88/44002
61. Ambroso, M.A., Kamien, R.D., Durian, D.J.: Dynamics of shallow impact cratering. Phys. Rev. E **72**, 041305 (2005). https://doi.org/10.1103/PhysRevE.72.041305
62. Jiang, M.J., Shen, Z.F., Wang, J.F.: A novel three-dimensional contact model for granulates incorporating rolling and twisting resistances. Comput. Geotech. **65**, 147–163 (2015). https://doi.org/10.1016/j.compgeo.2014.12.011